MULTIWAVELENGTH OBSERVATIONS AND MODELING OF 1ES 1959+650 IN A LOW FLUX STATE

E. ALIU[1], S. ARCHAMBAULT[2], T. ARLEN[3], T. AUNE[3], M. BEILICKE[4], W. BENBOW[5], R. BIRD[6], M. BÖTTCHER[7,8], A. BOUVIER[9],
V. BUGAEV[4], K. BYRUM[10], A. CESARINI[11], L. CIUPIK[12], E. COLLINS-HUGHES[6], M. P. CONNOLLY[11], W. CUI[13], R. DICKHERBER[4],
C. DUKE[14], J. DUMM[15], M. ERRANDO[1], A. FALCONE[16], S. FEDERICI[17,18], Q. FENG[13], J. P. FINLEY[13], G. FINNEGAN[19], L. FORTSON[15],
A. FURNISS[9], N. GALANTE[5], D. GALL[20], G. H. GILLANDERS[11], S. GRIFFIN[2], J. GRUBE[12], G. GYUK[12], D. HANNA[2], J. HOLDER[21],
G. HUGHES[17], T. B. HUMENSKY[22], P. KAARET[20], M. KERTZMAN[23], Y. KHASSEN[6], D. KIEDA[19], H. KRAWCZYNSKI[4], F. KRENNRICH[24],
M. J. LANG[11], A. S MADHAVAN[24], G. MAIER[17], P. MAJUMDAR[25,3], S. MCARTHUR[26], A. MCCANN[27], P. MORIARTY[28],
R. MUKHERJEE[1], T. NELSON[15], A. O'FAOLÁIN DE BHRÓITHE[6], R. A. ONG[3], M. ORR[24], A. N. OTTE[29], N. PARK[26], J. S. PERKINS[30,31],
A. PICHEL[32], M. POHL[18,17], A. POPKOW[3], H. PROKOPH[17], J. QUINN[6], K. RAGAN[2], L. C. REYES[33], P. T. REYNOLDS[34], E. ROACHE[5],
D. B. SAXON[21], M. SCHROEDTER[5], G. H. SEMBROSKI[13], C. SKOLE[17], A. W. SMITH[19], D. STASZAK[2], I. TELEZHINSKY[18,17],
M. THEILING[13], J. TYLER[2], A. VARLOTTA[13], V. V. VASSILIEV[3], S. P. WAKELY[26], T. C. WEEKES[5], A. WEINSTEIN[24], R. WELSING[17],
D. A. WILLIAMS[9], AND B. ZITZER[10]

[1] Department of Physics and Astronomy, Barnard College, Columbia University, NY 10027, USA
[2] Physics Department, McGill University, Montreal, QC H3A 2T8, Canada
[3] Department of Physics and Astronomy, University of California, Los Angeles, CA 90095, USA
[4] Department of Physics, Washington University, St. Louis, MO 63130, USA
[5] Fred Lawrence Whipple Observatory, Harvard-Smithsonian Center for Astrophysics, Amado, AZ 85645, USA
[6] School of Physics, University College Dublin, Belfield, Dublin 4, Ireland
[7] Astrophysical Institute, Department of Physics and Astronomy, Ohio University, Athens, OH 45701, USA
[8] Centre for Space Research, North-West University, Potchefstroom Campus, Potchefstroom 2531, South Africa
[9] Santa Cruz Institute for Particle Physics and Department of Physics, University of California, Santa Cruz, CA 95064, USA
[10] Argonne National Laboratory, 9700 South Cass Avenue, Argonne, IL 60439, USA
[11] School of Physics, National University of Ireland Galway, University Road, Galway, Ireland
[12] Astronomy Department, Adler Planetarium and Astronomy Museum, Chicago, IL 60605, USA
[13] Department of Physics, Purdue University, West Lafayette, IN 47907, USA
[14] Department of Physics, Grinnell College, Grinnell, IA 50112-1690, USA
[15] School of Physics and Astronomy, University of Minnesota, Minneapolis, MN 55455, USA
[16] Department of Astronomy and Astrophysics, 525 Davey Laboratory, Pennsylvania State University, University Park, PA 16802, USA
[17] DESY, Platanenallee 6, D-15738 Zeuthen, Germany
[18] Institute of Physics and Astronomy, University of Potsdam, D-14476 Potsdam-Golm, Germany
[19] Department of Physics and Astronomy, University of Utah, Salt Lake City, UT 84112, USA
[20] Department of Physics and Astronomy, University of Iowa, Van Allen Hall, Iowa City, IA 52242, USA
[21] Department of Physics and Astronomy and the Bartol Research Institute, University of Delaware, Newark, DE 19716, USA
[22] Physics Department, Columbia University, New York, NY 10027, USA
[23] Department of Physics and Astronomy, DePauw University, Greencastle, IN 46135-0037, USA
[24] Department of Physics and Astronomy, Iowa State University, Ames, IA 50011, USA
[25] Saha Institute of Nuclear Physics, 1/AF Bidhannagar, Sector-II, Kolkata-700064, India
[26] Enrico Fermi Institute, University of Chicago, Chicago, IL 60637, USA
[27] Kavli Institute for Cosmological Physics, University of Chicago, Chicago, IL 60637, USA
[28] Department of Life and Physical Sciences, Galway-Mayo Institute of Technology, Dublin Road, Galway, Ireland
[29] School of Physics and Center for Relativistic Astrophysics, Georgia Institute of Technology, 837 State Street NW, Atlanta, GA 30332-0430, USA
[30] CRESST and Astroparticle Physics Laboratory NASA/GSFC, Greenbelt, MD 20771, USA
[31] University of Maryland, Baltimore County, 1000 Hilltop Circle, Baltimore, MD 21250, USA
[32] Instituto de Astronomia y Fisica del Espacio, Casilla de Correo 67-Sucursal 28, (C1428ZAA) Ciudad Autnoma de Buenos Aires, Argentina
[33] Physics Department, California Polytechnic State University, San Luis Obispo, CA 94307, USA
[34] Department of Applied Physics and Instrumentation, Cork Institute of Technology, Bishopstown, Cork, Ireland

ABSTRACT

We report on the VERITAS observations of the high-frequency peaked BL Lac object 1ES 1959+650 in the period 2007–2011. This source is detected at TeV energies by VERITAS at 16.4 standard deviation (σ) significance in 7.6 hr of observation in a low flux state. A multiwavelength spectral energy distribution (SED) is constructed from contemporaneous data from VERITAS, *Fermi*-LAT, *RXTE* PCA, and *Swift* UVOT. *Swift* XRT data is not included in the SED due to a lack of simultaneous observations with VERITAS. In contrast to the orphan γ-ray flare exhibited by this source in 2002, the X-ray flux of the source is found to vary by an order of magnitude, while other energy regimes exhibit less variable emission. A quasi-equilibrium synchrotron self-Compton model with an additional external radiation field is used to describe three SEDs corresponding to the lowest, highest, and average X-ray states. The variation in the X-ray spectrum is modeled by changing the electron injection spectral index, with minor adjustments of the kinetic luminosity in electrons. This scenario produces small-scale flux variability of the order of $\lesssim 2$ in the high energy ($E > 1\,\mathrm{MeV}$) and very high energy ($E > 100\,\mathrm{GeV}$) γ-ray regimes, which is corroborated by the *Fermi*-LAT, VERITAS, and Whipple 10 m telescope light curves.

Key words: BL Lacertae objects: general – BL Lacertae objects: individual (1ES 1959+650 = VER J1959+651) – galaxies: active – gamma rays: galaxies

Online-only material: color figure

1

1. INTRODUCTION

Blazars are active galactic nuclei (AGNs) that appear bright from radio to γ-ray frequencies due to the close alignment of their relativistic jets along the line of sight of the observer. The blazar spectral energy distribution (SED) is characterized by a non-thermal double-peaked structure.

According to leptonic emission models, the low-energy peak (radio to UV or X-ray) is produced via synchrotron radiation of relativistic electrons in the jet. The high-energy (HE) peak (extending to TeV energies) is attributed either to the inverse-Compton up-scattering of the synchrotron photons by relativistic electrons (synchrotron self-Compton models; SSC) (e.g., Maraschi et al. 1992; Böttcher & Chiang 2002; Sokolov et al. 2004), or the up-scattering of photons external to the jet (external Compton models; EC) (e.g., Sikora et al. 1994; Dermer et al. 1992). The simplest SSC models are one-zone models, wherein the same population of electrons that produce the synchrotron radiation up-scatter the photons. Multi-component SSC models also exist and allow for the presence of multiple electron populations.

BL Lac objects are a subset of blazars characterized by nonthermal continuum emission without emission lines, and strong, rapid variability. They may be divided into three classes based on the position of the synchrotron peak in frequency space (Padovani & Giommi 1995). High-frequency peaked BL Lac objects (HBLs) exhibit synchrotron peak emission at UV–X-ray frequencies, intermediate-frequency peaked BL Lac objects show synchrotron peak emission at optical–UV frequencies, and low-frequency peaked BL Lac objects have their synchrotron peak emission in IR–optical bands.

The HBL 1ES 1959+650, discovered in 1993 with redshift $z = 0.047$ (Schachter et al. 1993) was later found to be a source of TeV emission (Holder et al. 2003; Nishiyama 1999). It has previously exhibited dramatic very high energy (VHE; $E > 100\,GeV$) flaring episodes, most notably on 2002 June 4, when a γ-ray flare without an increase in X-ray emission was detected from the source, providing the first unambiguous example of an "orphan" γ-ray flare (Krawczynski et al. 2004; Holder et al. 2003; Daniel et al. 2005). Krawczynski et al. (2004) modeled this orphan flare with a simple SSC model and found that this underpredicted the observed radio and optical fluxes. The authors examined mechanisms for producing an orphan γ-ray flare in the context of a SSC model and found that it could not be explained by one-zone SSC models. Multi-component SSC models may account for orphan γ-ray flares either through an extra low-energy electron population or a second high-density electron population confined to a small emission volume. Sokolov et al. (2004) showed that it is also possible for flares to occur with frequency-dependent time lags through shock collision in the blazar jet. Hadronic models were also developed as alternative models for this event (Böttcher 2005).

In this article, we report on multiwavelength observations of 1ES 1959+650 from UV to VHE γ-rays during the period 2007–2011. We consider the source in a low flux state during the sampling of observations covered here due to a mean recorded VHE γ-ray flux of 23% of the Crab Nebula flux. On 2012 May 20, the Very Energetic Radiation Imaging Telescope Array System (VERITAS) observed a rapid VHE flare from 1ES 1959+650, to be presented in E. Aliu et al. (in preparation). Section 2 of this article describes the observations and data analyses, and the results of the multiwavelength SED modeling

are presented in Section 3. A discussion of these results and their implications is given in Section 4.

2. MULTIWAVELENGTH OBSERVATIONS AND ANALYSIS

2.1. VERITAS

The VERITAS is an array of four 12 m diameter imaging atmospheric Cherenkov telescopes (IACTs) located at the base of Mt. Hopkins in southern Arizona. Each telescope in the array is composed of 350 hexagonal mirror facets and a 499 pixel photomultiplier tube (PMT) camera at the focal plane with a field of view (FoV) of $\sim 3^\circ.5$ and angular resolution of $0^\circ.15$ (Holder et al. 2008). The array operates in the energy range ~ 0.1–50 TeV, with an energy resolution of $\sim 15\%$ at VHEs.

The VERITAS observations of 1ES 1959+650 were carried out between 2007 November 13 and 2011 October 28 (MJD 54417 − 55862) as part of a routine blazar program monitoring for enhanced emission. The source never met the threshold criteria for target of opportunity (ToO) observations during enhanced VHE emission, so only minimal monitoring data were taken.

The data were taken in *wobble mode*, with a $0^\circ.5$ offset from the source position in each of the four cardinal directions alternately so that the background can be estimated from simultaneously gathered data, and systematic effects in the background estimation cancel out (Aharonian et al. 2001; Berge et al. 2007). Observations were conducted in a range of zenith angles 34°–53° using the full four-telescope array, giving a total of 7.6 hr of live time on the source.

The data are analyzed using the latest release of the analysis software described in Cogan (2008). The images are first flat-fielded using information from nightly calibration runs taken with a pulsed UV LED light source (Hanna et al. 2010). The images are then cleaned using a form of the picture/boundary method (Daniel 2008). Next, the images are parameterized (Hillas 1985). Finally, the shower directions are reconstructed from the data in each telescope and a set of selection criteria is applied to reject background events such as cosmic rays, as described in Krawczynski et al. (2006).

In this analysis, images composed of fewer than five pixels are rejected. For each image, *mean scaled width* and *mean scaled length* parameters (the average of the widths and lengths of the γ-ray ellipses in each telescope scaled by an expected value based on simulations) are required to be in the range 0.05–1.15 and 0.05–1.3, respectively (Konopelko et al. 1999). The altitude of the maximum Cherenkov emission from the reconstructed shower is required to be higher than 7 km above the array. A circular region of radius $0^\circ.1$ centered on the source coordinates is defined from which γ-ray like events are selected. The results presented here have all been confirmed using an independent secondary analysis package, described in Daniel (2008).

For the low elevation observations of 1ES 1959+650, the energy threshold is found to increase to $\sim 800\,GeV$, from $\sim 100\,GeV$ achievable at higher elevations. All VERITAS fluxes are therefore quoted above 1 TeV. 1ES 1959+650 is detected at $16.4\,\sigma$ with an average flux of $(3.97 \pm 0.37) \times 10^{-12}$ photons cm^{-2} s^{-1} (or $(7.54 \pm 0.7) \times 10^{-12}$ erg cm^{-2} s^{-1}, equivalent to $\sim 23\%$ Crab Nebula flux) above 1 TeV. This corresponds to 268 excess γ-rays at the source location at R.A. $= 19^h59^m59^s \pm 20^s_{\rm stat}$ and decl. $= 65^\circ.9'.25 \pm 0'.34_{\rm stat}$ (J2000 coordinates). The observed VERITAS signal is consistent with a point source, and the source is designated VER J1959+651.
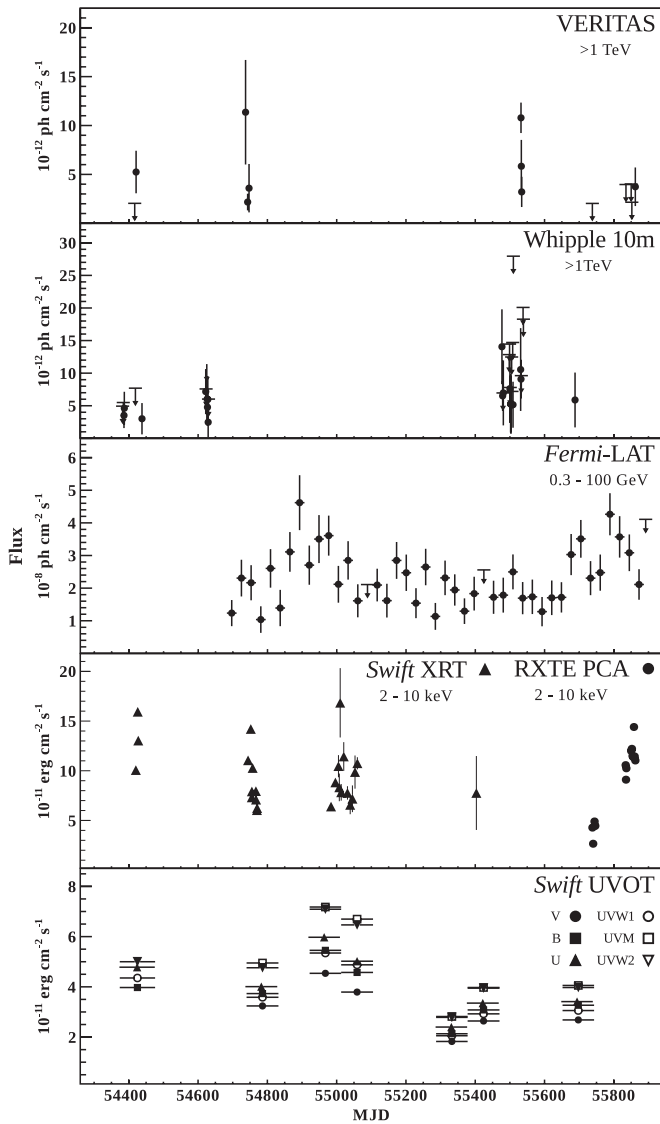
Figure 1. Light curves of 1ES 1959+650 in all energy bands analyzed for this paper. VERITAS and Whipple light curves are displayed in nightly bins; the *Fermi*-LAT light curve is shown in four week bins; *RXTE* PCA and *Swift* XRT are binned by observation, the duration of which can vary; the *Swift* UVOT light curve is in 90 day bins. Strong variability is seen in the X-ray regime on the order of 48 hr from the *RXTE* observations (panel 4), however, this timescale is dominated by the time between observations. Other wavebands exhibit more stable emission, with γ-rays (panels 1–3) showing variability on the order of ~2. For VERITAS and Whipple data sets, upper limits are calculated for points with a significance $<1\sigma$. For *Fermi*-LAT, upper limits are calculated for bins with $TS < 3$.

A nightly light curve is shown in the top panel of Figure 1. A constant flux is fit to the light curve, using the low significance flux points instead of the upper limit values. This yields $\chi^2/\mathrm{NDF} = 5.37$ and fit probability 3.43×10^{-9}, providing $>5\sigma$ evidence for flux variability. It can be seen that the variability amplitude with respect to the average is of order ~2.

A time-averaged differential spectrum, shown in Figure 2, is constructed from the entire data set, and is fit with a power law of form $dN/dE = N(E/E_0)^{-\Gamma}$ where E_0 is the pivot energy and is set at 1 TeV. The fit parameters are $N = (6.12 \pm 0.53_{\mathrm{stat}} \pm 2.45_{\mathrm{sys}}) \times 10^{-12}\,\mathrm{cm}^{-2}\,\mathrm{s}^{-1}\,\mathrm{TeV}^{-1}$, $\Gamma = 2.54 \pm 0.08_{\mathrm{stat}} \pm 0.3_{\mathrm{sys}}$, with $\chi^2/\mathrm{NDF} = 1.25$ and a fit probability of 0.28.
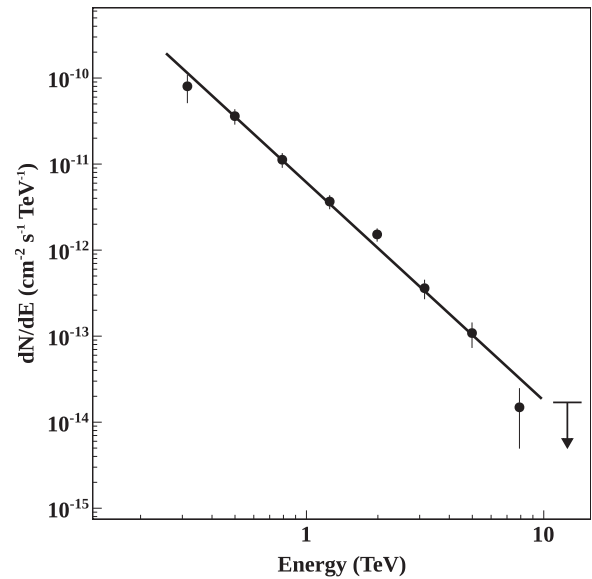

Figure 2. VERITAS time-averaged differential spectrum of 1ES 1959+650 fit with a power law of form $dN/dE = N(E/E_0)^{-\Gamma}$; $N = (6.12 \pm 0.53_{\mathrm{stat}} \pm 2.45_{\mathrm{sys}}) \times 10^{-12}\,\mathrm{cm}^{-2}\,\mathrm{s}^{-1}\,\mathrm{TeV}^{-1}$, $\Gamma = 2.54 \pm 0.08_{\mathrm{stat}} \pm 0.3_{\mathrm{sys}}$, and $E_0 = 1$ TeV.

2.2. Whipple 10 m Telescope

The Whipple 10 m γ-ray telescope is an IACT also located on Mt. Hopkins in southern Arizona. It operated continuously from 1968 until it was decommissioned in the summer of 2011. The reflector was composed of 248 tessellated hexagonal mirror facets with a total reflecting area of ~75 m². The focal plane camera was improved many times over the lifetime of the telescope, and in its last configuration it consisted of 379 PMTs and had a FoV of ~2.°6 with an angular resolution of 0.°12, corresponding to camera configuration **g** described in Kildea et al. (2007).

The Whipple 10 m telescope observed 1ES 1959+650 between 2007 October 9 and 2008 June 13 (MJD 54382 − 54630) and again between 2010 October 8 and 2011 May 7 (MJD 55477 − 55688). The data were taken in *tracking mode*, whereby the telescope points directly at the source and slews to track it across the sky for the duration of the observation, and the background is estimated from the region of the FoV not toward the source location. The source was observed in a range of zenith angles 35°–57° for a total of 28 hr live time.

The data are analyzed using the standard Supercuts procedure as described in Appendix B of Reynolds et al. (1993). For large zenith angle (LZA; $> 35°$) observations, the γ-ray selection criteria are adjusted to account for the change in detector performance. The values of the *width* and *length* cuts are adjusted using the results of the Monte Carlo simulations of Krennrich et al. (1997). As 1ES 1959+650 has a spectral index comparable to that of the Crab Nebula, standard and LZA observations of the Crab Nebula in 2007/2008 are used as calibration data sets on which to optimize the *trigger* selection cuts. No LZA Crab Nebula data are available for 2010/2011, so the scaling that is found between the standard and LZA cuts in 2007/2008 is applied to the standard 2010/2011 *trigger* cuts to produce LZA cuts for that season. The energy threshold of the instrument is found to increase to ~920 GeV at LZA, from ~400 GeV at standard observing angles. The *dist* cut is required to be in the range 0.°5–0.°8.

During its last years of operation, the Whipple 10 m telescope operated as a dedicated blazar monitor with the aim of triggering stereoscopic observations of sources showing interesting or increased activity with the VERITAS array. 1ES 1959+650 was one of the sources routinely monitored in this program, and on 2010 December 2 (MJD 55532), the Whipple 10 m observed it in an apparent state of elevated emission. The VERITAS array was alerted and ToO observations were taken. While it was confirmed that the measured flux was greater than average by a factor of $\sim$2 ($\sim$50% Crab Nebula flux), the increase was not sufficient to deem the source to be in an exceptional flaring state.

1ES 1959+650 is detected at $6.2\,\sigma$ in the entire data set with an average flux of $(5.27 \pm 0.73) \times 10^{-12}$ photons cm^{-2} s^{-1} (or $(9.74 \pm 1.3) \times 10^{-12}$ erg cm^{-2} s^{-1}) above 1 TeV (assuming a spectral index of 2.4), corresponding to 211 excess γ-rays at the source location. A nightly light curve is shown in the second panel of Figure 1. Fitting this with a constant flux yields a $\chi^2/\mathrm{NDF} = 0.53$ with a fit probability of 0.94.

2.3. Fermi-LAT

The Large Area Telescope (LAT) is a pair production telescope, sensitive above $\sim$20 MeV, and is the primary instrument on board the *Fermi* satellite (Atwood et al. 2009). It consists of three main components; the converter, the tracker and the calorimeter. The converter comprises 16 layers of tungsten in which incident photons pair produce. The converter is interwoven with single-sided silicon strip detectors that constitute the tracker, allowing the measurement of the positions of the charged particles in each layer. The calorimeter is positioned beneath the converter/tracker, and measures the energy of the particle shower which results from the electron/positron pair. For the effective rejection of cosmic rays, the system is covered with an anti-coincidence shield. The primary observation mode of *Fermi* is sky-survey mode, in which the satellite rocks about the zenith, maximizing the sky-coverage of the LAT while maintaining near-uniform exposure.

Analysis is performed on all *Fermi*-LAT observations of 1ES 1959+650 since the satellite's launch through 2011 December 2 (MJD 54682−55897). Events are extracted from a region of interest (ROI) of radius 10° centered on the coordinates of 1ES 1959+650. Events from the *diffuse class* with zenith angle <100° and energy in the range 0.3–100 GeV are selected. Data taken when the rocking angle of the spacecraft is greater than 52° are discarded to avoid contamination from photons from Earth's limb. Source significance and spectral parameters are computed using an unbinned likelihood analysis with the LAT Science Tools.[35]

A background model including all γ-ray sources from the *Fermi*-LAT second source catalog (2FGL; Nolan et al. 2012) within 12° of 1ES 1959+650 is created. Remaining excesses in the ROI are modeled as point sources with a simple power law spectrum. The spectral parameters of sources within the ROI are left free during the minimization process. The galactic and extragalactic diffuse γ-ray emission as well as the residual instrumental background are included using the recommended model files.[36]

A light curve is calculated in four week bins and is shown in the third panel of Figure 1. Flux variability up to a factor of $\sim$2 above the mean is evident; fitting the light curve with a
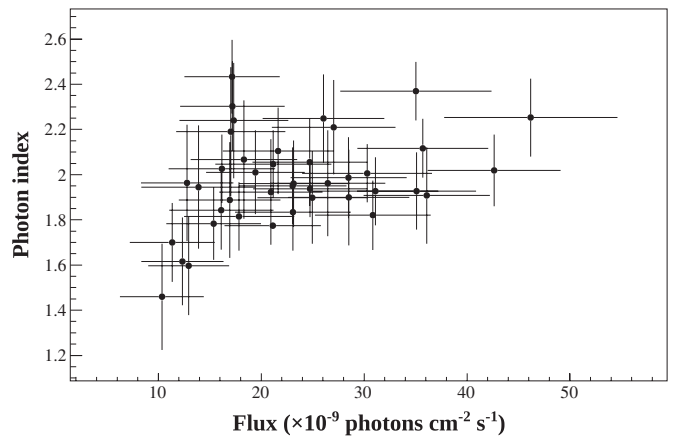

Figure 3. Flux–index correlation of *Fermi*-LAT data. The Pearson product–moment correlation coefficient is found to be 0.37 ± 0.15, implying a medium level of linear correlation.

constant flux gives a $\chi^2/\mathrm{NDF} = 2.26$ and a fit probability of 9.24×10^{-6}. The data are then rebinned into four week bins centered on VERITAS observations, and data from intervening periods without VERITAS observations are removed. This contemporaneous data set shows no evidence of variability with a constant flux fit yielding $\chi^2/\mathrm{NDF} = 1.33$ and a fit probability of 0.26.

The source is detected with a test statistic of $2620(\simeq 50\,\sigma)$ with an average flux of $(2.16 \pm 0.09) \times 10^{-8}$ photons cm^{-2} s^{-1} (or $(1.89 \pm 0.08) \times 10^{-11}$ erg cm^{-2} s^{-1}). A flux–index correlation study is performed on the entire data set, the result of which is shown in Figure 3. The Pearson product–moment correlation coefficient is found to be 0.37 ± 0.15 implying a medium level of linear correlation.

A differential spectrum is produced from the entire data set and a second spectrum is constructed from the contemporaneous data set. Both are fit with a power law of form $dN/dE = N(E/E_0)^{-\Gamma}$ where E_0 is the pivot energy and is set at 1402.26 MeV, and are found to be fully consistent. Parameters obtained from the whole data set are $N = (3.33 \pm 0.12) \times 10^{-12}$ cm^{-2} s^{-1} MeV^{-1}, $\Gamma = 1.99 \pm 0.03$. Parameters for the contemporaneous data set are $N = (3.34 \pm 0.72) \times 10^{-12}$ cm^{-2} s^{-1} MeV^{-1}, $\Gamma = 1.98 \pm 0.18$. These results are similar to the 2FGL values of $N = (2.9 \pm 0.12) \times 10^{-12}$ cm^{-2} s^{-1} MeV^{-1} and $\Gamma = 1.94 \pm 0.03$.

2.4. RXTE PCA

The *Rossi X-ray Timing Explorer* (*RXTE*) operated from a low-earth circular orbit from 1995 December 30 to 2012 January 5. The Proportional Counter Array (PCA) on board *RXTE* consisted of five large detectors each with three xenon gas-filled signal detection layers with anti-coincidence side and rear chambers and a propane top layer (Bradt et al. 1993). It was sensitive over the energy range 2–60 keV with an energy resolution of 18% at 6 keV. The X-ray shielded hexagonal tubular collimators provided a 1° FWHM FoV.

The PCA data set comprises observations of 1ES 1959+650 during the period 2011 June 26 to 2011 October 28 (MJD 55738 − 55862). Analysis of PCA data is performed on *Standard-1 mode* data following the RXTE Cook Book[37]

---

[35] ScienceTools-v9r23p1 with P7SOURCE_V6 instrument response function.
[36] gal_2yearp7v6_v0, iso_p7v6clean

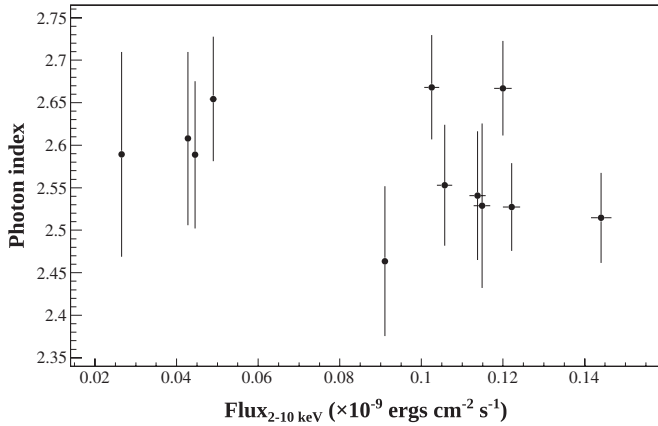[37] http://heasarc.nasa.gov/docs/xte/recipes/cook_book.html

Figure 4. Flux–index plot of *RXTE* PCA data showing no significant variation of photon index with flux level.

Figure 5. Flux–index plot of *Swift* XRT data showing no significant variation of photon index with flux levels.

Figure 6. Time-average differential spectrum measured with *Swift* XRT in the range 0.3–10 keV, fit with a photo-absorbed power law of form $dN/dE = \exp[-n_{\rm H}\,\sigma(E)]\,N(E/E_0)^{-\Gamma}$; $n_{\rm H} = (1.57 \pm 0.05) \times 10^{21}$, $N = (6.36 \pm 0.12) \times 10^{-2}\,{\rm cm}^{-2}\,{\rm s}^{-1}\,{\rm keV}^{-1}$, and $\Gamma = 2.4 \pm 0.02$.

using the HEASoft[38] and XSPEC[39] packages. A deadtime correction factor is calculated individually for each observation. A light curve binned by observation (durations vary between $\sim$1.1 and $\sim$4.1 ks) is shown in the fourth panel of Figure 1 and exhibits flux variability of a factor of $\sim$4 throughout the data set. This variability is seen on the timescale of 48 hr, dominated by the time between observations. No significant variability within single observations is present. The photon index is found to be constant for all flux levels (see Figure 4), with a fit with constant index yielding $\chi^2/{\rm NDF} = 1.17$ and a fit probability of 0.29.

A differential time-averaged spectrum is produced from the top layer only and fit in the range 3–10 keV with a power law of the form $dN/dE = KN(E/E_0)^{-\Gamma}$ where K is a multiplicative constant to correct for deadtime and $E_0 = 1$ keV. A single deadtime correction factor of 1.02 is calculated for the entire data set and frozen during the fitting process. Fit results are $N = (7.27 \pm 0.23) \times 10^{-2}\,{\rm cm}^{-2}\,{\rm s}^{-1}\,{\rm keV}^{-1}$ and $\Gamma = 2.63 \pm 0.02$ with $\chi^2/{\rm NDF} = 1.76$.

An average differential spectrum is also produced using only the three observations of 1ES 1959+650 that are truly simultaneous with VERITAS observations. The model parameters are found to be $N = (7.90 \pm 0.46) \times 10^{-2}\,{\rm cm}^{-2}\,{\rm s}^{-1}\,{\rm keV}^{-1}$ and $\Gamma = 2.58 \pm 0.04$ in agreement with the full time-averaged spectral parameters, with an improved goodness-of-fit, $\chi^2/{\rm NDF} = 1.23$.

2.5. Swift XRT

The X-Ray Telescope (XRT) on board *Swift* is a Wolter type 1 telescope with a FoV of $23' \times 23'$ and an energy range of 0.2–10 keV (Burrows et al. 2005). It has an effective area of 120 cm^2 at 1.5 keV and angular resolution of $18''$.

Swift XRT observations of 1ES 1959+650 taken in *photon counting mode* are analyzed. A correction for pile-up is applied individually to each observation by fitting a King function (King 1971) to the data and using an annular source selection region, the inner radius of which is set to the value at which the fit and data diverge for that particular observation. This analysis is completed using the same HEASoft and XSPEC packages as in Section 2.4. A light curve binned by observation is produced, and the flux and flux variability is found to be consistent with results from *RXTE* PCA. This light curve is shown in the fourth panel of Figure 1, showing variability over the course of the
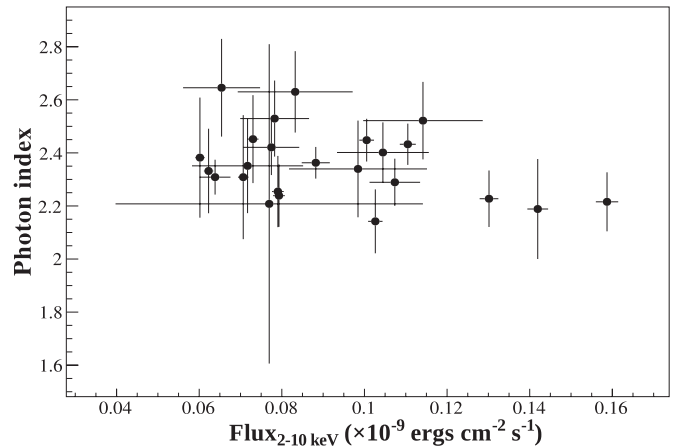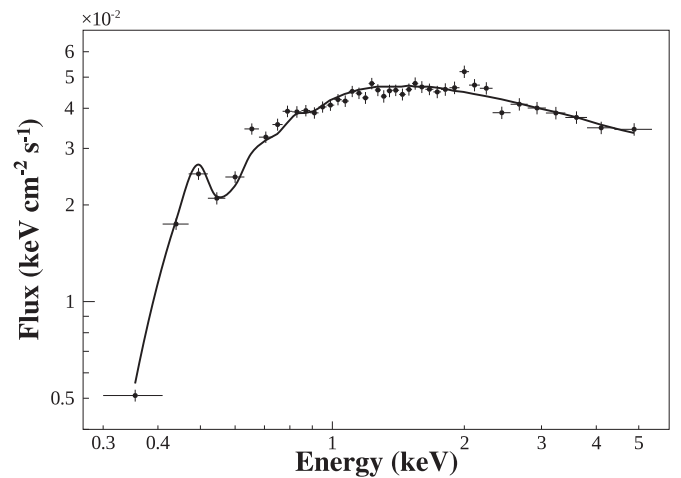
observations up to a factor of $\sim$3. As with *RXTE* PCA data, the photon index is found to be stable for all flux levels (see Figure 5) with a fit with constant index yielding $\chi^2/{\rm NDF} = 0.93$ and a fit probability of 0.55.

No XRT observations of 1ES 1959+650 occurred simultaneously with VERITAS observations, so only one time-averaged differential spectrum (see Figure 6) is produced and binned with 500 events per bin. The spectrum is fit in the range 0.3–10 keV ignoring all bad channels with a photo-absorbed power law of form $dN/dE = \exp[-n_{\rm H}\,\sigma(E)]\,N(E/E_0)^{-\Gamma}$. Free parameters are returned as $n_{\rm H} = (1.57 \pm 0.05) \times 10^{21}$, $N = (6.36 \pm 0.12) \times 10^{-2}\,{\rm cm}^{-2}\,{\rm s}^{-1}\,{\rm keV}^{-1}$, and $\Gamma = 2.4 \pm 0.02$ with $\chi^2/{\rm NDF} = 1.677$. The galactic hydrogen density obtained from this fit is larger than the measured value of 1.0×10^{21} reported in Kalberla et al. (2005). Freezing the $n_{\rm H}$ parameter to the value of Kalberla et al. (2005) degrades the goodness-of-fit (in this case $\chi^2/{\rm NDF} = 5.76$). It is found that a photo-absorbed log parabolic model does not provide a better fit than the original power law model, yielding a $\chi^2/{\rm NDF} = 1.720$.

2.6. Swift UVOT

The UltraViolet and Optical Telescope (UVOT), which is co-aligned with the XRT, has a 30 cm mirror with f-number

---

[38] HEASoft version 6.11.1
[39] XSPEC version 12.7

12.7 (Roming et al. 2005). Light from the mirror is focused onto 2 identical detectors, each of which has an 11 position filter wheel, giving the instrument an effective range of 170–600 nm.

The UVOT data analysis is performed on all observations in the period 2007 January 1 to 2012 April 1 (MJD 54101−56018). Exposures are taken in V, B, U, UVW1, UVM2, and UVW2 pass bands in *image mode*, discarding the photon timing information. The photometry is computed using an aperture of $5''$ following the general prescriptions of Poole et al. (2008) and Breeveld et al. (2010) and introducing an annular background region (inner and outer radii of $20''$ and $30''$ respectively). The background light contamination arising from nearby sources is removed by introducing "ad hoc" exclusion regions.

The results are reddening corrected using $E(B - V) = 0.185$, (Schlegel et al. 1998). The optical/UV galactic extinction coefficients are computed ($R_V = 3.9$) and applied (Fitzpatrick 1999). The host galaxy contribution of 1ES 1959+650 is estimated using the PEGASE-HR code (Le Borgne et al. 2004) extended for the ultraviolet UVOT filters and by using the R band photometric results of Nilsson et al. (2007).

The redshift of 1ES 1959+650 means that the possibility of intergalactic absorption/extinction cannot be excluded. However, an estimate of this value has not been pursued here—its quantification is still a matter of debate, particularly at UV wavelengths. No correction for zodiacal light is introduced in this analysis.

For each filter, the integrated flux is computed using the effective frequency and not convolving the filter transmission with the source spectrum. In the case of 1ES 1959+650, this may produce a moderate overestimation ($\sim$10%) of the integrated flux, so the total systematic uncertainty is then $\sim$15%.

A light curve in 90 day bins for each waveband is shown in the bottom panel of Figure 1.

3. BROADBAND SED MODELING

Multiwavelength SEDs are constructed from VERITAS, *Fermi*-LAT, *RXTE* PCA, and *Swift* UVOT data. The time-averaged spectrum from the entire VERITAS data set provides the VHE γ-ray information. While there is evidence for flux variability in the VERITAS observations, there are not enough data to produce time-resolved spectra. Also, the *Fermi*-LAT data contemporaneous with VERITAS shows no evidence of variability, indicating that the entire inverse-Compton component of the SED is likely to be stable.

The spectrum from the *Fermi*-LAT data set contemporaneous with VERITAS is used, removing any bias in this part of the SED due to flux variability; there is clear variability over the course of the entire LAT data set whereas the LAT data set contemporaneous with VERITAS shows no evidence of variability.

Due to the coarse binning of the UVOT data, no attempt was made to extract regions (quasi-) simultaneous with VERITAS, and so a time-averaged spectrum from the entire data set was used. While this may introduce a slight systematic bias on the statistical error at low energies, it is not expected that this should alter the main result of the modeling.

Significant variability is observed in the *RXTE* PCA X-ray data, even within the three observations that were taken simultaneously with VERITAS observations. However, as the X-ray statistics are high, it is feasible to create spectra for the individual observations, as well as an average spectrum from the three observations. It is found that the photon index is consistent within errors for the different X-ray spectra, but the normalization is variable.

Three broadband SEDs are then formed, differing only in the X-ray regime; one SED with the highest normalization X-ray spectrum, one with the lowest normalization X-ray spectrum, and one using the average X-ray spectrum. This provides the opportunity to investigate the possible cause of large variability in X-rays with fairly steady emission in other regimes, which is in contrast to the orphan γ-ray variability previously observed in this source.

The SEDs are modeled using a purely leptonic SSC model (described in Acciari et al. (2009), which is a quasi-equilibrium version of the model of Böttcher & Chiang (2002)) with the addition of an external radiation field that is isotropic in the rest frame of the AGN (EC component). The EC component is necessary, as a simple single-zone SSC model cannot reproduce the shallow *Fermi*-LAT spectrum due to curvature from strong Klein–Nishina effects.

Briefly, the SSC component assumes that a population of ultrarelativistic leptons is injected into a spherical emitting volume (the blob) of radius R_B in the comoving frame which moves at a relativistic speed $\beta_\Gamma c$ corresponding to the bulk Lorentz factor Γ. The size of the blob is constrained by the shortest observed variability timescale $\delta t_{\rm var,min}$ through $R_B \leqslant c\delta t_{\rm var,min} D/(1 + z)$. The injected population is described by an injection power L_e and a single power law spectral shape of index q with low- and high-energy cutoffs, $\gamma_{\rm min}$ and $\gamma_{\rm max}$, respectively. An equilibrium between the particle injection, radiative cooling, and the escape of particles from the blob gives rise to a temporary quasi-equilibrium state described by a broken power law. Particle escape is specified through an escape time parameter $\eta_{\rm esc}$ where $t_{\rm esc} = \eta_{\rm esc}(R/c)$. The external radiation field is characterized by blackbody emission from dust at a temperature $T_{\rm BB}$ and with energy density $u_{\rm ext}$ around the central AGN engine. Due to the low energy of these external seed photons, Klein–Nishina effects are expected to be negligible.

Due to the lack of constraints on the observing angle $\theta_{\rm obs}$ between the jet and the line-of-sight, $\theta_{\rm obs}$ is set to be the superluminal angle, for which Γ is equal to the Doppler factor $D(= (\Gamma[1 - \beta_\Gamma \cos \theta_{\rm obs}])^{-1})$. The magnetic field B in the blob is a free parameter. The Poynting flux along the jet is denoted by L_B, and the equipartition parameter is given by L_B/L_e.

A standard flat ΛCDM cosmology is assumed, with $\Omega_m = 0.3$ and $\Omega_\Lambda = 0.7$. The effect of EBL absorption is accounted for using the model of Finke et al. (2010).

A set of parameters is derived for each of the three X-ray states (high, low, and average), and it is found that the X-ray variability can be modeled by changing almost exclusively the electron injection spectral index, with minor adjustments of the kinetic luminosity in electrons. The models provide a reasonable representation of the data, but tend to underestimate the flux at a few hundred MeV. The data and models are shown in Figure 7. The parameters of the models are shown in Table 1.

4. DISCUSSION

The parameters for these models are chosen to reproduce the significant X-ray variability recorded during simultaneous observations of low flux and marginally variable γ-ray observations. In contrast with most other models for this source (with the exception of Tavecchio et al. 2010), a scenario in which the electrons and magnetic field are in equipartition is favored. The X-rays are produced by the highest-energy electrons, but the VHE γ-rays are produced by significantly lower-energy electrons. In order to create this scenario where the VHE electrons produce the X-rays, a low magnetic field and high Doppler
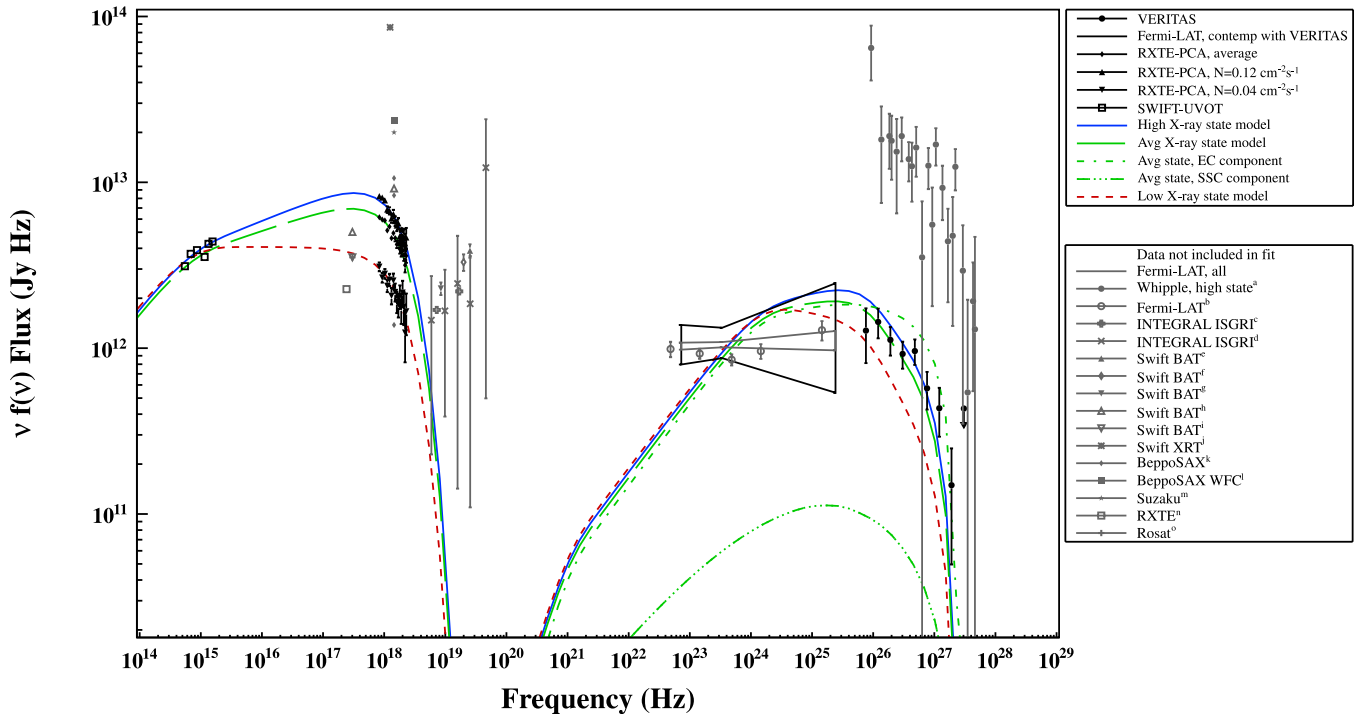
Figure 7. Leptonic SSC+EC models for the three SEDs. The *Fermi*-LAT spectrum produced in this work is represented by butterfly plots (gray for the time-averaged spectrum, black for the contemporaneous spectrum), while data points are used for all other instruments. The solid (blue) line corresponds to the model for the highest X-ray normalization, the dotted (red) line shows the model for the lowest X-ray normalization, and the dashed (green) line represents the model for the time-averaged X-ray spectrum. Archival data are shown in gray for comparison.[a]Daniel et al. (2005); [b]Nolan et al. (2012); [c]Beckmann et al. (2009); [d]Bottacini et al. (2010); [e]Tueller et al. (2010); [f]Cusumano et al. (2010); [g]Ajello et al. (2009); [h]Winter et al. (2009); [i]Tavecchio et al. (2010); [j]Maselli et al. (2010); [k]Donato et al. (2005); [l]Verrecchia et al. (2007); [m]Tagliaferri et al. (2008); [n]Resconi et al. (2009); [o]Massaro et al. (2009).

(A color version of this figure is available in the online journal.)

Table 1
Parameters of SSC+EC Models for the Three Multiwavelength SEDs
Corresponding to the Highest, Lowest, and Time-averaged X-Ray States

Parameter	High X-Ray	Low X-Ray	Avg. X-Ray
γ_{min}	1.8×10^4	1.8×10^4	1.8×10^4
γ_{max}	9×10^5	9×10^5	9×10^5
q	1.7	2.0	1.75
η_{esc}	1000	1000	1000
B at z_0(G)	0.02	0.02	0.02
Γ	30	30	30
R_B (cm)	1.5×10^{17}	1.5×10^{17}	1.5×10^{17}
θ_{obs} (°)	1.91	1.91	1.91
T_{BB} (K)	20	20	20
u_{ext} (erg cm^{-3})	3.5×10^{-10}	3.5×10^{-10}	3.5×10^{-10}
$\delta t_{var,min}$ (s)[a]	1.74×10^5	1.74×10^5	1.74×10^5
L_e (erg s^{-1})	3.28×10^{43}	3.27×10^{43}	3.03×10^{43}
L_B (erg s^{-1})	3.04×10^{43}	3.04×10^{43}	3.04×10^{43}
L_B/L_e	0.93	0.93	1.0

Notes. [a] This parameter is not constrained by these observations; while the *RXTE* observations show variability on this timescale, it is dominated by the time between observations. However, it is a reasonable estimate in this low-state case with no evidence for rapid variability.

factor is required, differing from the models presented in previous work, e.g., Tagliaferri et al. (2008) and Tavecchio et al. (2010). With this setup it is easy to generate de-coupled HE variability, such as the "anti-orphan" X-ray variability seen in this case, or the "orphan" γ-ray flare observed in 2002. De-coupled X-ray flares can be created by hardening the electron

spectrum, or VHE flares produced by injecting additional electrons at lower energies.

It is also of note that the X-ray to optical flux ratio observed in this case is lower than has been reported previously in the literature. A substantial break is therefore needed around optical wavelengths in this model in order to connect to the X-rays, whereas the other SEDs are consistent with a smooth continuum through the optical–UV to X-rays. As a result, a steeper electron spectrum is required here than is presented in other works.

The very hard electron injection spectral indices ($1.7 \leqslant q \leqslant 2.0$) pose challenges to standard models of ultrarelativistic Fermi acceleration at parallel shocks. These models can produce indices in the range $2.2 \lesssim q \lesssim 2.3$ (Achterberg et al. 2001). This may indicate the presence of other processes such as acceleration at oblique subluminal shocks which are capable of producing hard electron indices in the presence of large-angle scattering (Summerlin & Baring 2012), stochastic acceleration (second-order Fermi acceleration) (Virtanen & Vainio 2005), or particle acceleration at shear boundary layers in the case of an inhomogeneous jet with a fast inner spine and slow outer cocoon (Ostrowski 2000; Stawarz & Ostrowski 2002; Rieger & Duffy 2004).

The external Compton component on a thermal blackbody used in this model is motivated by the known presence of dust in the central environment of 1ES 1959+650 (Fumagalli et al. 2012). In order to maintain scattering in the Thomson regime, the temperature of this dust is constrained to be very cold ($T_{BB} = 20$ K). Even with this, the inverse-Compton peak does not provide an accurate representation of the *Fermi*-LAT spectrum.

These observations show that 1ES 1959+650 can be reasonably well-described by a leptonic quasi-equilibrium SSC + EC model in a low VHE flux state, although it is clear that this model does not account for the flux observed at a few hundred MeV to $\sim$1 GeV and as such, does not provide an accurate representation of the inverse-Compton peak. The model parameters obtained here cannot be fully explained by first-order Fermi acceleration at parallel shocks, and instead may suggest particle acceleration at oblique subluminal shocks, or that 1ES 1959+650 may consist of an inhomogeneous jet with a fast inner spine and slower-moving outer cocoon.

REFERENCES

Acciari, V. A., Aliu, E., Aune, T., et al. 2009, ApJ, 707, 612
Achterberg, A., Gallant, Y. A., Kirk, J. G., & Guthmann, A. W. 2001, MNRAS, 328, 393
Aharonian, F., Akhperjanian, A., Barrio, J., et al. 2001, A&A, 370, 112
Ajello, M., Costamante, L., Sambruna, R. M., et al. 2009, ApJ, 699, 603
Atwood, W. B., Abdo, A. A., Ackermann, M., et al. 2009, ApJ, 697, 1071
Beckmann, V., Soldi, S., Ricci, C., et al. 2009, A&A, 505, 417
Berge, D., Funk, S., & Hinton, J. 2007, A&A, 466, 1219
Bottacini, E., Böttcher, M., Schady, P., et al. 2010, ApJL, 719, L162
Böttcher, M. 2005, ApJ, 621, 176
Böttcher, M., & Chiang, J. 2002, ApJ, 581, 127
Bradt, H. V., Rothschild, R. E., & Swank, J. H. 1993, A&AS, 97, 355
Breeveld, A. A., Curran, P. A., Hoversten, E. A., et al. 2010, MNRAS, 406, 1687
Burrows, D. N., Hill, J. E., Nousek, J. A., et al. 2005, SSRv, 120, 165
Cogan, P. 2008, in Proc. of 30th International Cosmic Ray Conference, Vol. 3, ed. R. Caballero, J. C. D'Olivo, G. Medina-Tanco, L. Nellen, F. A. Sánchez, & J. F. Valdés-Galicia, 1385
Cusumano, G., La Parola, V., Segreto, A., et al. 2010, A&A, 524, A64
Daniel, M. K. 2008, in Proc. of 30th International Cosmic Ray Conference, Vol. 3, ed. R. Caballero, J. C. D'Olivo, G. Medina-Tanco, L. Nellen, F. A. Sánchez, & J. F. Valdés-Galicia, 1325
Daniel, M. K., Badran, H. M., Bond, I. H., et al. 2005, ApJ, 621, 181
Dermer, C. D., Schlickeiser, R., & Mastichiadis, A. 1992, A&A, 256, L27
Donato, D., Sambruna, R. M., & Gliozzi, M. 2005, A&A, 433, 1163
Finke, J. D., Razzaque, S., & Dermer, C. D. 2010, ApJ, 712, 238
Fitzpatrick, E. L. 1999, PASP, 111, 63
Fumagalli, M., Dessauges-Zavadsky, M., Furniss, A., et al. 2012, MNRAS, 424, 2276
Hanna, D., McCann, A., McCutcheon, M., & Nikkinen, L. 2010, NIMPA, 612, 278
Hillas, A. M. 1985, in Proc. of 19th International Cosmic Ray Conference, Vol. 3, ed. F. C. Jones, 445
Holder, J., Acciari, V. A., Aliu, E., et al. 2008, in AIP Conf. Proc. 1085, High Energy Gamma-ray Astronomy, ed. F. A. Aharonian, W. Hoffmann, & F. Rieger (Melville, NY: AIP), 657
Holder, J., Bond, I. H., Boyle, P. J., et al. 2003, ApJL, 583, L9
Kalberla, P. M. W., Burton, W. B., Hartmann, D., et al. 2005, A&A, 440, 775
Kildea, J., Atkins, R., Badran, H., et al. 2007, APh, 28, 182
King, I. R. 1971, PASP, 83, 199
Konopelko, A., Hemberger, M., Aharonian, F., et al. 1999, APh, 10, 275
Krawczynski, H., Carter-Lewis, D. A., Duke, C., et al. 2006, APh, 25, 380
Krawczynski, H., Hughes, S. B., Horan, D., et al. 2004, ApJ, 601, 151
Krennrich, F., Akerlof, C. W., Buckley, J. H., et al. 1997, ApJ, 481, 758
Le Borgne, D., Rocca-Volmerange, B., Prugniel, P., et al. 2004, A&A, 425, 881
Maraschi, L., Ghisellini, G., & Celotti, A. 1992, ApJL, 397, L5
Maselli, A., Cusumano, G., Massaro, E., et al. 2010, A&A, 520, A47
Massaro, E., Giommi, P., Leto, C., et al. 2009, A&A, 495, 691
Nilsson, K., Pasanen, M., Takalo, L. O., et al. 2007, A&A, 475, 199
Nishiyama, T. 1999, in Proc. of 26th International Cosmic Ray Conference, Vol. 3, ed. B. L. Dingus, D. B. Kieda, & M. H. Salamon (Melville, NY: AIP), 370
Nolan, P. L., Abdo, A. A., Ackermann, M., et al. 2012, ApJS, 199, 31
Ostrowski, M. 2000, MNRAS, 312, 579
Padovani, P., & Giommi, P. 1995, ApJ, 444, 567
Poole, T. S., Breeveld, A. A., Page, M. J., et al. 2008, MNRAS, 383, 627
Resconi, E., Franco, D., Gross, A., Costamante, L., & Flaccomio, E. 2009, A&A, 502, 499
Reynolds, P. T., Akerlof, C. W., Cawley, M. F., et al. 1993, ApJ, 404, 206
Rieger, F. M., & Duffy, P. 2004, ApJ, 617, 155
Roming, P. W. A., Kennedy, T. E., Mason, K. O., et al. 2005, SSRv, 120, 95
Schachter, J. F., Stocke, J. T., Perlman, E., et al. 1993, ApJ, 412, 541
Schlegel, D. J., Finkbeiner, D. P., & Davis, M. 1998, ApJ, 500, 525
Sikora, M., Begelman, M. C., & Rees, M. J. 1994, ApJ, 421, 153
Sokolov, A., Marscher, A. P., & McHardy, I. M. 2004, ApJ, 613, 725
Stawarz, L., & Ostrowski, M. 2002, ApJ, 578, 763
Summerlin, E. J., & Baring, M. G. 2012, ApJ, 745, 63
Tagliaferri, G., Foschini, L., Ghisellini, G., et al. 2008, ApJ, 679, 1029
Tavecchio, F., Ghisellini, G., Ghirlanda, G., Foschini, L., & Maraschi, L. 2010, MNRAS, 401, 1570
Tueller, J., Baumgartner, W. H., Markwardt, C. B., et al. 2010, ApJS, 186, 378
Verrecchia, F., in't Zand, J. J. M., Giommi, P., et al. 2007, A&A, 472, 705
Virtanen, J. J. P., & Vainio, R. 2005, ApJ, 621, 313
Winter, L. M., Mushotzky, R. F., Reynolds, C. S., & Tueller, J. 2009, ApJ, 690, 1322